

Article

Not peer-reviewed version

---

# Effect of Support on Steam Reforming of Ethanol for H<sub>2</sub> Production with Copper-Based Catalysts

---

[Ramiro Picoli Nippes](#) , [Paula Derksen Macruz](#) , [Aline Domingues Gomes](#) , Marcos de Souza ,  
Bruna Rodrigues Ferreira , Roberta Carolina Pelissari Rizzo-Domingues , [Luiz Pereira Ramos](#) \*

Posted Date: 30 May 2024

doi: 10.20944/preprints202405.2026.v1

Keywords: Ethanol steam reforming; Hydrogen production; Copper-based catalysts; Zeolite; Mixed oxides



Preprints.org is a free multidiscipline platform providing preprint service that is dedicated to making early versions of research outputs permanently available and citable. Preprints posted at Preprints.org appear in Web of Science, Crossref, Google Scholar, Scilit, Europe PMC.

Copyright: This is an open access article distributed under the Creative Commons Attribution License which permits unrestricted use, distribution, and reproduction in any medium, provided the original work is properly cited.

Disclaimer/Publisher's Note: The statements, opinions, and data contained in all publications are solely those of the individual author(s) and contributor(s) and not of MDPI and/or the editor(s). MDPI and/or the editor(s) disclaim responsibility for any injury to people or property resulting from any ideas, methods, instructions, or products referred to in the content.

## Article

# Effect of Support on Steam Reforming of Ethanol for H<sub>2</sub> Production with Copper-Based Catalysts

Ramiro Picoli Nippes <sup>1</sup>, Paula Derksen Macruz <sup>2</sup>, Aline Domingues Gomes <sup>2</sup>, Marcos de Souza <sup>2</sup>, Bruna Rodrigues Ferreira <sup>3</sup>, Roberta Carolina Pelissari Rizzo-Domingues <sup>3</sup> and Luiz Pereira Ramos <sup>1,\*</sup>

<sup>1</sup> Graduate Program in Chemical Engineering, Federal University of Paraná, R. Francisco H. dos Santos, Curitiba, 81531-990, Paraná, Brazil; ramiro\_picoli@yahoo.com.br; luiz.ramos@ufpr.br

<sup>2</sup> Department of Chemical Engineering, Maringá State University, Av. Colombo, 5790, Maringá, 87020-900, Paraná, Brazil; pauladmacruz@gmail.com; alinedgs@gmail.com; msouza2@uem.br

<sup>3</sup> Department of Chemical and Biology, Federal Technology University of Paraná, Av. Heitor de Alencar Furtado, 5000, Curitiba, 81280-340, Paraná, Brazil; bruna1.ferreira@yahoo.com.br; robertac@utfpr.edu.br

\* Correspondence: luiz.ramos@ufpr.br; Tel.: +55(41)99963-6084

**Abstract:** Catalytic studies for hydrogen production via steam reforming of ethanol (SRE) are essential for process optimization. Likewise, selecting the ideal support for the active phase can be critical to achieve high conversion rates during the catalytic steam reforming. In this work, copper-based catalysts were synthesized using two different supports, NaY zeolite and Nb<sub>2</sub>O<sub>5</sub>/Al<sub>2</sub>O<sub>3</sub> mixed oxides. The materials were prepared using wet impregnation and characterized for their physicochemical properties using different analytical techniques. Differences in catalyst morphologies were readily attributed to the characteristics of the support. The Cu/NaY catalyst showed better textural properties than Cu/Nb<sub>2</sub>O<sub>5</sub>/Al<sub>2</sub>O<sub>3</sub>, resulting in a homogeneous metal dispersion over the support surface. Both catalytic systems were active in SRE, but Cu/NaY resulted in higher ethanol conversions compared to Cu/Nb<sub>2</sub>O<sub>5</sub>/Al<sub>2</sub>O<sub>3</sub>. Hence, the performance of copper-based catalysts was influenced significantly by the textural properties of the support.

**Keywords:** ethanol steam reforming; hydrogen production; copper-based catalysts; zeolite; mixed oxides

## 1. Introduction

The increasing global demand for energy, coupled with the socioenvironmental impacts of an energy matrix that is still heavily reliant on traditional fossil fuels such as coal, crude oil, and natural gas [1,2], are crying out for the development of sustainable production processes to support the transition to a new and more diversified energy matrix. Among the sustainable alternatives for this energy transition, hydrogen (H<sub>2</sub>) stands out as one of the most prominent.

H<sub>2</sub> can be obtained through different pathways such as electrolysis [3,4], biological reactions [5], biomass gasification [6], steam reforming [7,8], and partial oxidation of both hydrocarbons and alcohols [9]. Among these possibilities, the use of ethanol as feedstock for H<sub>2</sub> production in fuel cells has considerable advantages. These include easier storage, handling, and safe transportation due to its low toxicity and volatility. Additionally, ethanol is a renewable feedstock when obtained through biomass fermentation, is rich in H<sub>2</sub>, and has a nearly closed carbon cycle that helps in the abatement of greenhouse gas emissions [10,11]. Thus, the steam reforming of ethanol (SRE) emerges as an attractive solution for H<sub>2</sub> production due to its high H<sub>2</sub> yield and thermodynamic feasibility [12].

SRE for H<sub>2</sub> production is a catalytic process. Therefore, H<sub>2</sub> yield depends on the properties of the catalyst to be employed [13]. This includes the catalytic support for the active phase [14] and the method used for catalyst preparation [15]. In general, the catalyst design is crucial for a successful SRE process. Different catalytic systems have been investigated for SRE using noble and non-noble metal-based catalysts [16]. Among them, copper-based catalysts [17–19] have the advantage of being

cost-effective and widely available compared to other metals. Additionally, the presence of copper active sites promotes ethanol steam reforming to produce H<sub>2</sub> and CO or its dehydrogenation to acetaldehyde followed by decarbonylation, producing CH<sub>4</sub> and CO [20–22]. Hence, copper-based catalysts have potential for SRE applications.

The choice of support for the active phase is extremely important for SRE because it plays a significant role in H<sub>2</sub> selectivity and catalyst stability [23,24]. In general, efficient SRE supports must have favorable textural properties and moderate acidity, in addition to being relatively cheap, readily available, and easily accessible. In this study, two supports were selected and evaluated for their effect on H<sub>2</sub> production by SRE using copper as the catalytic active phase.

The first selected support was NaY, a commercially available zeolite that is known for its high heat resistance, unique ordered three-dimensional porous structure, and larger pores compared to the dimensions of the ethanol molecule, as well as low production costs [25,26]. For instance, NaY can be synthesized from alternative, abundant, and inexpensive materials such as rice husks [27,28] and wheat straw [29] ashes. Several studies have already demonstrated the application of NaY as a catalyst support for SER [30–32]. The other selected support was a Nb<sub>2</sub>O<sub>5</sub>/Al<sub>2</sub>O<sub>3</sub> mixed oxide. Alumina is a widely used as a support in heterogeneous catalysis [33–37] due to its large surface area, good stability, and wide commercial availability [38]. Nb<sub>2</sub>O<sub>5</sub> is also a notable material in the field of catalysis, known for its non-toxic nature, suitable acid properties [39,40], excellent chemical stability, high thermodynamic stability, low cost, and high commercial availability [41,42]. The combination of Nb<sub>2</sub>O<sub>5</sub> with alumina is favorable because, being an n-type semiconductor, Nb<sub>2</sub>O<sub>5</sub> can interact with copper in catalytic active reaction sites [43,44]. Additionally, Nb<sub>2</sub>O<sub>5</sub> is structurally similar to commercial catalysts for methanol reforming (Cu/ZnO/Al<sub>2</sub>O<sub>3</sub>). Since ZnO is also an n-type semiconductor oxide, Nb<sub>2</sub>O<sub>5</sub> may have similar catalytic properties.

This study aimed to evaluate the effect of both NaY and Nb<sub>2</sub>O<sub>5</sub>/Al<sub>2</sub>O<sub>3</sub> supports on H<sub>2</sub> production by SRE using copper as the catalytic active phase. Copper was anchored on the support surface by wet impregnation. Then, the obtained catalysts were characterized using several analytical techniques and subjected to SRE using an experimental reaction module.

## 2. Materials and Methods

### 2.1. Material

Materials were synthesized using copper nitrate (Cu(NO<sub>3</sub>)<sub>2</sub>·3H<sub>2</sub>O, 98%) from Sigma-Aldrich, commercial alumina (Al<sub>2</sub>O<sub>3</sub>, 90%) from Merck, NaY zeolite from Sigma-Aldrich, and niobic acid (HY-340) from the Brazilian Metallurgy and Mining Company (CBMM). HY-340 was heat-treated to obtain niobium pentoxide (Nb<sub>2</sub>O<sub>5</sub>).

### 2.2. Methods

#### 2.2.1. Catalyst Preparation

The catalysts were prepared using a simple wet impregnation methodology under solvent excess, consisting of the following steps: initially, appropriate quantities of the copper precursor (Cu(NO<sub>3</sub>)<sub>2</sub>·3H<sub>2</sub>O) were dissolved in water and mixed with the support (NaY or Nb<sub>2</sub>O<sub>5</sub>/Al<sub>2</sub>O<sub>3</sub>) in a rotary evaporator. The mixture was evaporated for 2 h at 343 K for complete water evaporation. After this, the materials were placed in an oven at 353 K for about 10 h. Then, the dried materials were crushed and subjected to a thermal treatment in a muffle furnace at 773.15 K for 5 h, using a heating rate of 10 K min<sup>-1</sup>. At the end of the process, two catalysts named Cu/NaY and Cu/ Nb<sub>2</sub>O<sub>5</sub>/Al<sub>2</sub>O<sub>3</sub> were obtained.

#### 2.2.2. Catalyst Characterization

Scanning Electron Microscopy (SEM) was performed using a Zeiss EVO MA15 microscope coupled with an X-Max 20 mm<sup>2</sup> Energy Dispersive Spectrometer (EDS). X-ray Diffraction (XRD) analyses were conducted on a Shimadzu XDR-7000 diffractometer using CuK $\alpha$  radiation.

Measurements were taken at 40 kV and 30 mA using a Cu tube with a wavelength of 1.54 nm, with a scan rate of  $2^\circ \text{ min}^{-1}$  and an interval of  $5^\circ \leq 2\theta \leq 80^\circ$ . The FWHM of the XRD peaks was used to estimate the average particle size using the Scherrer equation (Eq. 1).

$$D_{(hkl)} = \frac{0.9 \times \lambda}{\beta_{(hkl)} \times \theta'} \quad (1)$$

The textural properties of the catalysts were determined by  $\text{N}_2$  adsorption/desorption at 77 K using a NOVA-4000-Quantachrome adsorption analyzer. Infrared spectroscopy analyses (FTIR) were performed using a Varian 640-IR spectrometer with potassium bromide (KBr) as the dispersing agent in the region from 4000 to 400  $\text{cm}^{-1}$ . Temperature-programmed desorption of  $\text{NH}_3$  (TPD- $\text{NH}_3$ ) and Temperature-programmed reduction (TPR) were carried out using a Quantachrome Chembet-3000 multi-use unit coupled with a ThermoStar-GSD 301 mass spectrometer. In both analyses, 0.1 g sample was placed in a "U"-shaped quartz reactor, which was first subjected to a 20  $\text{cm}^3/\text{min}$   $\text{N}_2$  flow at 300°C for 1 h to remove humidity and possibly adsorbed materials. For TPD- $\text{NH}_3$  analysis, the samples were reduced with 1.75%  $\text{H}_2$  diluted in  $\text{N}_2$  for 1 h using a heating rate of 10°C/min from room temperature to 500°C and remaining at this temperature for another 1 h.  $\text{NH}_3$  adsorption was performed at 100°C for 30 min with a flow rate of 15  $\text{cm}^3/\text{min}$  of 5%  $\text{NH}_3$  diluted in  $\text{N}_2$ . Subsequently, the system was purged for 2 h with a flow rate of 20  $\text{cm}^3/\text{min}$   $\text{N}_2$ . Finally, the sample was heated to 700°C at a heating rate of 10°C/min under  $\text{N}_2$  flow for  $\text{NH}_3$  desorption. TPR was performed with a reducing gas feed containing 1.75%  $\text{H}_2$  in  $\text{N}_2$  at a flow rate of 20  $\text{cm}^3/\text{min}$ , from room temperature to 1000°C with a heating rate of 10°C/min.

### 2.2.3. Catalytic Performance Evaluation

SRE was carried out using two catalysts, Cu/NaY and Cu/ $\text{Nb}_2\text{O}_5/\text{Al}_2\text{O}_3$ . Tests were performed in an experimental unit consisting of a preheating system, a 20 cm long stainless-steel reactor with an internal diameter of 2.54 cm, a condenser, and a phase collector/sePARATOR. The reactant mixture was introduced through the system inlet using a peristaltic pump.

Before the catalytic tests, the catalysts were activated *in situ* with an 85  $\text{cm}^3/\text{min}$   $\text{N}_2$  flow rate containing 40%  $\text{H}_2$  by volume using the following heating steps: 30 min at 100°C, 1 h at 200°C, and 4 h at 500°C. After this, the  $\text{H}_2$  flow was stopped, and the  $\text{N}_2$  flow was adjusted to 85 mL/min for 4 h to purge  $\text{H}_2$  from the entire reaction system. Subsequently, catalytic tests were conducted at 300°C and 450°C using a mass hourly space velocity of 40  $\text{dm}^3/\text{h.g}_{\text{cat}}$ , 5 g catalyst (40 mesh, positioned at the center with the reactor ends filled with silica of the same particle size), and a  $\text{H}_2\text{O}/\text{C}_2\text{H}_5\text{OH}$  molar ratio of 10/1 without the presence of an inert. The gaseous products were analyzed in a Trace GC ThermoQuest gas chromatograph with a Carboxen 1010 PLOT column, with argon as carrier gas, detection by TCD, and the following temperature programming: 7 min at 45°C; 25°C/min to 180°C; and 5 min at 180°C. The liquid phase was analyzed using a Varian 3300 gas chromatograph, with a 10% Carbowax 20M CHR W HP column, helium as carrier gas, detection by TCD, and the following temperature programming: 2 min at 50°C; 25°C/min to 100°C; and 2 min at 100°C.

Evaluation of catalytic performance for  $\text{H}_2$  production and product selectivity (dry basis) were based on ethanol conversion following Eqs. (2) and (3),

$$C_{\text{EtOH}}(\%) = \left( \frac{F_{\text{in}}^{\text{EtOH}} - F_{\text{out}}^{\text{EtOH}}}{F_{\text{in}}^{\text{EtOH}}} \right) \times 100, \quad (2)$$

$$S_i(\%) = \sum_i \left( \frac{n_i}{n_t} \right) \times 100 \quad (3)$$

where  $F$  is the molar flow rate,  $n_i$  is the average molar flow rate of the product component,  $i$  is the component of the mixture, and  $n_t$  is the average molar flow rate of the products, excluding water.

## 3. Results and Discussion

### 3.1. Catalyst Characterization

### 3.1.1. Morphology

SEM was used to analyze the microstructural morphology of the catalysts. Figure 1a shows the NaY support, and Figure 1b the synthesized Cu/NaY catalyst. Even after the wet impregnation of copper on the NaY support, the polyhedral shapes of the zeolite remained regular and homogeneous, indicating no change in its morphological structure. By contrast, Figure 1c shows the Nb<sub>2</sub>O<sub>5</sub> support while Figure 1d shows the synthesized Cu/Nb<sub>2</sub>O<sub>5</sub>/Al<sub>2</sub>O<sub>3</sub> catalyst. Unlike Cu/NaY, the particles are randomly distributed with various geometries and distinct sizes. These morphological properties were attributed to the nature of the support used, which does not present a well-defined microstructural morphology and evenly distributed particle sizes.

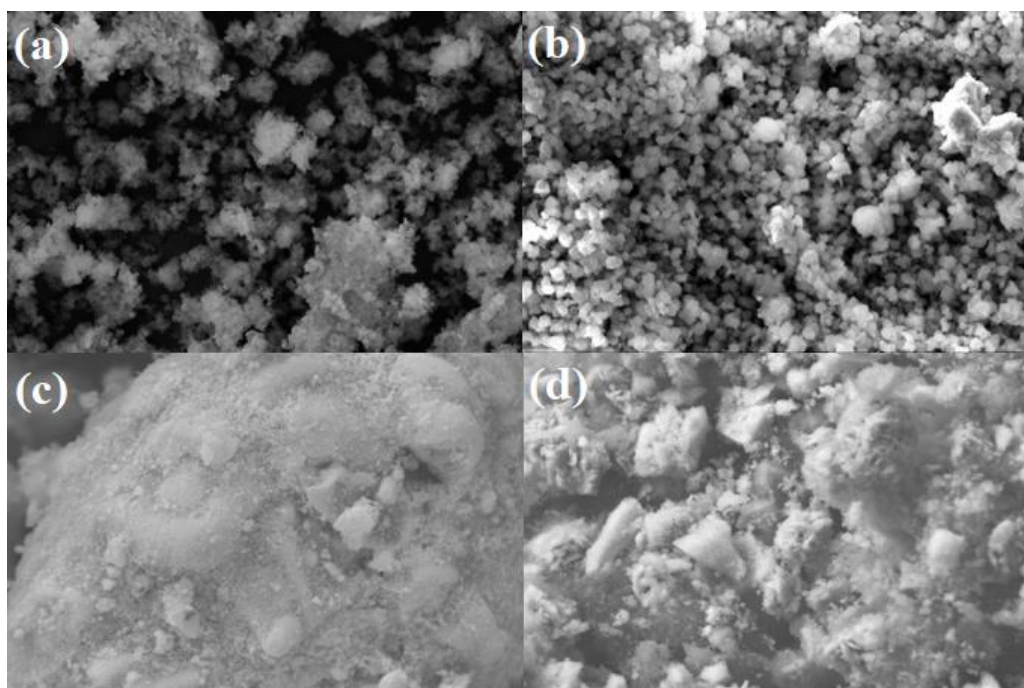


**Figure 1.** SEM at 4000x of (a) NaY, (b) Cu/NaY, (c) Nb<sub>2</sub>O<sub>5</sub> and (d) Cu/Nb<sub>2</sub>O<sub>5</sub>/Al<sub>2</sub>O<sub>3</sub>.

Elemental mapping was performed by EDS to identify chemical elements at the catalyst surface, using a magnification of 4,000x. Figure 2 shows that all proposed elements were detected, indicating the effectiveness of the proposed wet impregnation process. Additionally, Cu seemed to be better dispersed on NaY compared to Nb<sub>2</sub>O<sub>5</sub>/Al<sub>2</sub>O<sub>3</sub>, which presented higher Cu concentration in some regions. This is strongly linked to the superior textural properties of the zeolite, which allowed for a better distribution of the metal particles.

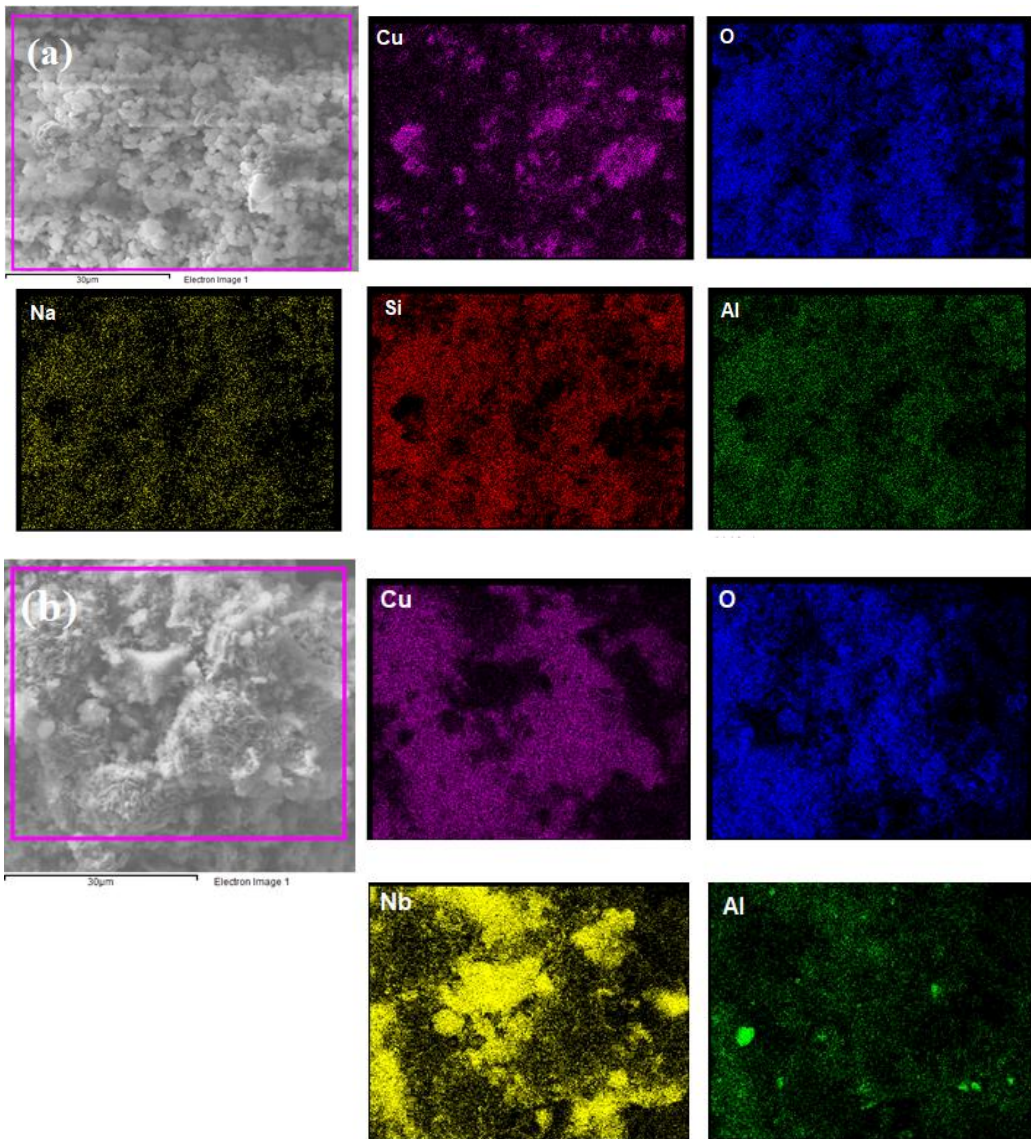


**Figure 2.** Elemental mapping of (a) Cu/NaY and (b) Cu/Nb<sub>2</sub>O<sub>5</sub>/Al<sub>2</sub>O<sub>3</sub>.

Table 1 presents the EDS mass composition of the catalysts. Cu was present in both catalysts in very similar percentages. Furthermore, a Si/Al ratio of 2.58 confirmed the presence of unmodified NaY zeolite after the wet impregnation synthesis.

**Table 1.** Elemental analysis of Cu/NaY and Cu/Nb<sub>2</sub>O<sub>5</sub>/Al<sub>2</sub>O<sub>3</sub>.

Sample	Element (%)						
	Cu	Na	Al	Si	O	Nb	C
Cu/NaY	11.90	3.87	3.00	7.76	26.75	-	3.01
Cu/Nb <sub>2</sub> O <sub>5</sub> /Al <sub>2</sub> O <sub>3</sub>	11.17	-	2.84	-	15.72	10.82	0.88

### 3.1.2. Crystallinity

The XRD technique was employed to determine the crystallinity and purity of the synthesized catalysts. The experimental XRD patterns obtained for Cu/NaY and Cu/Nb<sub>2</sub>O<sub>5</sub>/Al<sub>2</sub>O<sub>3</sub> are shown in Figure 3. For the Cu/NaY catalyst, the diffraction peaks at  $2\theta = 6.18^\circ, 15.61^\circ, 18.66^\circ, 23.64^\circ, 26.98^\circ$ , and  $31.36^\circ$  are indexed to the cubic crystal structure of NaY, which corresponds to the Fd-3m space group in card #00-039-1380. The diffraction peaks at  $2\theta = 35.57^\circ, 38.72^\circ, 48.81^\circ, 58.30^\circ, 61.60^\circ, 66.32^\circ$ , and  $68.12^\circ$  are indexed to the monoclinic crystal system of CuO, referring to card #01-089-5895. The X-ray

diffractogram of the Cu/NaY catalyst indicated that there were no modifications in the original crystal structure of the zeolite, probably due to the fine distribution of copper on the zeolite structure [45].

The Cu/Nb<sub>2</sub>O<sub>5</sub>/Al<sub>2</sub>O<sub>3</sub> catalyst presented diffraction peaks at  $2\theta = 35.57^\circ, 38.72^\circ, 48.81^\circ$ , and  $56.72^\circ$ , which are indexed to the monoclinic crystal system of CuO in card #01-089-5895. The diffraction peak at  $2\theta = 67.03^\circ$  is indexed to the hexagonal crystal system of Al<sub>2</sub>O<sub>3</sub> in card #00-013-0373, while the diffraction peaks at  $2\theta = 22.60^\circ, 28.58^\circ, 36.71^\circ$ , and  $46.23^\circ$  are indexed to the hexagonal crystal system of Nb<sub>2</sub>O<sub>5</sub> in card #00-028-0317. Both copper oxide and niobium pentoxide are present in the diffractogram with significant intensities, indicating that the precursors maintained their defined crystal lattice even after the catalyst synthesis. Also, alumina diffraction peaks are almost imperceptible, indicating a high dispersion of alumina in niobium oxide [46].

The crystallite size has important implications for the rate of molecular diffusion and the contribution of the external surface area to adsorption and desorption rates. For the calculation of the crystallite size of the active phase in both catalysts, the (-111) diffraction peak at  $2\theta = 35.57^\circ$  of copper oxide was considered. The result was approximately 55 nm for both catalysts, indicating that the change of support did not cause alteration in the crystallite size of the active phase. For the calculation of the support crystallite sizes, the (533) diffraction peak at  $2\theta = 23.64^\circ$  of NaY and the (100) diffraction peak at  $2\theta = 28.58^\circ$  of Nb<sub>2</sub>O<sub>5</sub> were considered, resulting in 114 nm and 43 nm, respectively. Kugai et al. [47] concluded that the smaller the crystallite size of the support, the greater the dispersion of the active phase and consequently the higher the catalytic activity, indicating that the catalyst performance strongly depends on surface area and crystallite sizes.

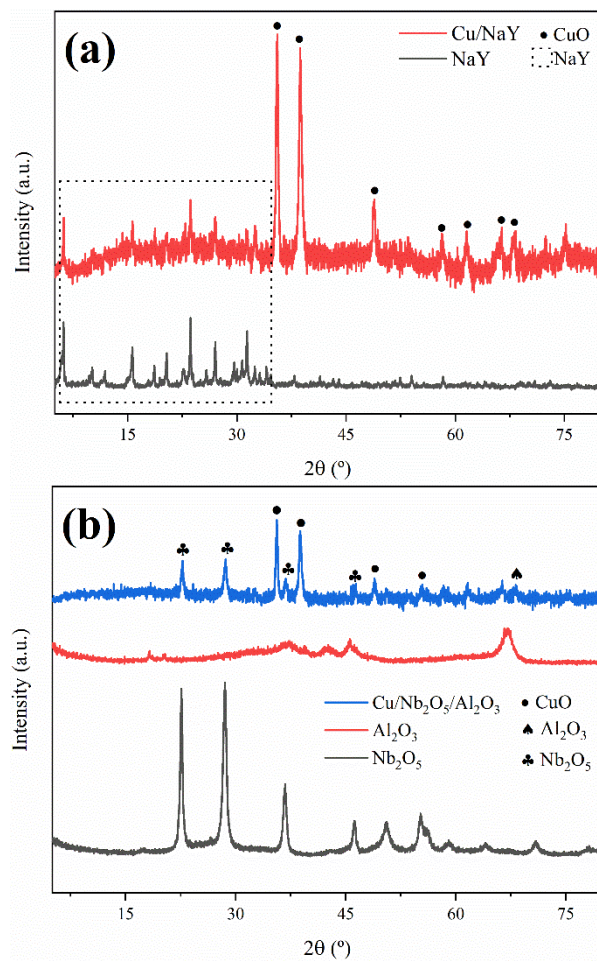
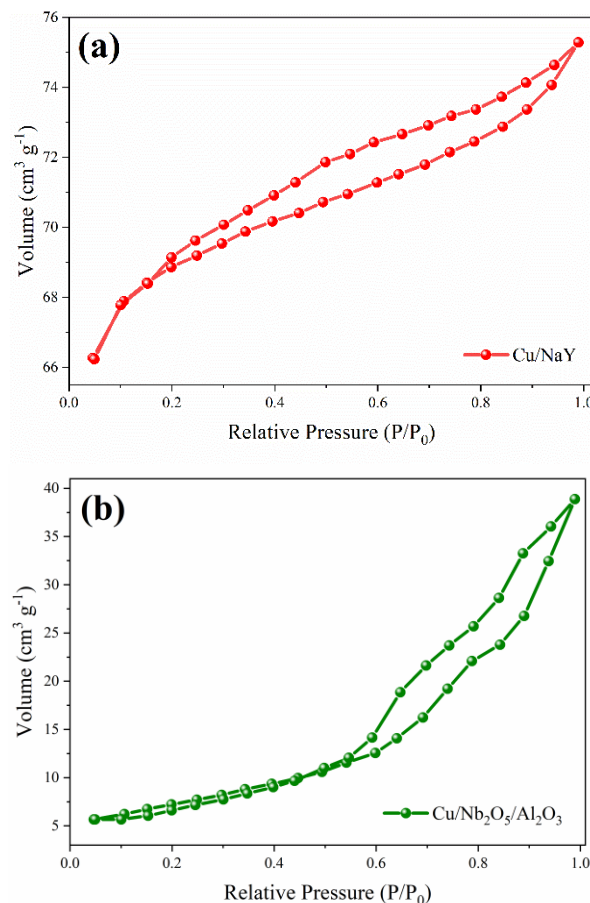


**Figure 3.** DRX patterns of (a) Cu/NaY and (b) Cu/Nb<sub>2</sub>O<sub>5</sub>/Al<sub>2</sub>O<sub>3</sub>.

### 3.1.3. Textural Parameters

The determination of textural parameters of the synthesized materials and their precursors is relevant to understand their SRE catalytic performance. The parameters obtained through  $N_2$  physisorption are presented in Table 2, while the  $N_2$  adsorption/desorption isotherms are shown in Figure 4. For the Cu/NaY catalyst, the isotherm exhibits characteristics of type IV according to I.U.P.A.C. [48], which is attributed to the presence of micropores associated with mesopores. The formation of a round knee-like feature at the beginning of the isotherm is related to the formation of adsorbed  $N_2$  monolayers inside micropores [49], while the increase in relative pressure improves adsorption as the material mesopores are filled. For the Cu/Nb<sub>2</sub>O<sub>5</sub>/Al<sub>2</sub>O<sub>3</sub> catalyst, the obtained isotherm is of type V, which is also associated with mesoporous materials with weak adsorbate-adsorbent interactions. In both isotherms, there was hysteresis in  $N_2$  desorption, which is characteristic of capillary condensation in mesoporous materials [50]. For Cu/NaY, the hysteresis of type H4 is associated with narrow slit-like pores, while for Cu/Nb<sub>2</sub>O<sub>5</sub>/Al<sub>2</sub>O<sub>3</sub>, the hysteresis of type H3 refers to non-rigid aggregates of plate-like particles forming slit pores, typical of non-uniform pore sizes and shapes as observed by SEM.

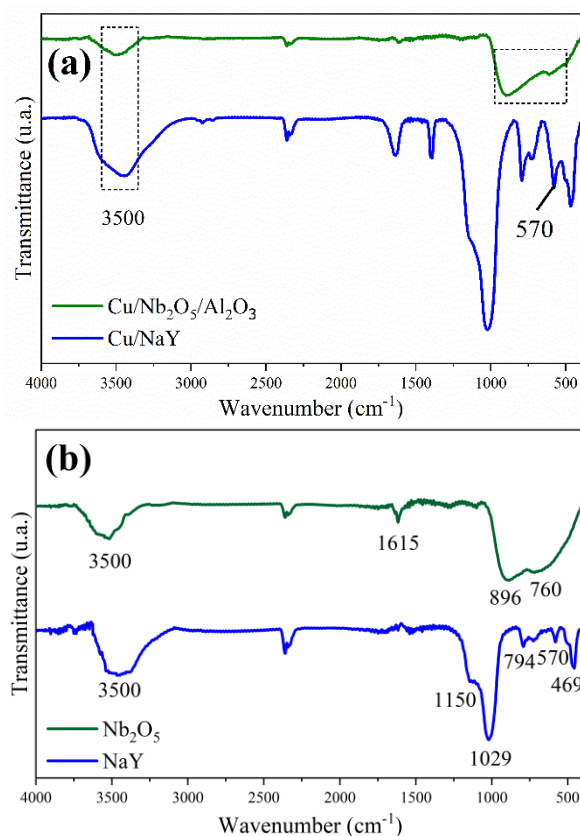
Concerning the obtained values for textural parameters, the surface areas of the catalytic supports were similar to other studies involving NaY [51,52], Nb<sub>2</sub>O<sub>5</sub> [10,42] and Al<sub>2</sub>O<sub>3</sub> [53,54]. For the catalysts, a noticeable reduction in surface area and pore volume was observed, compared to their corresponding precursors. This effect is strongly associated with the possible obstruction of smaller pore diameters (micropores) by deposition of copper oxides inside the catalyst structure, as evidenced by the reduction in micropore volume. However, despite this reduction, a significant variation in textural properties was detected among our catalysts. This reinforces the possible influence of the support type on the catalyst performance, as it plays a fundamental role in the reaction. Cu/NaY has a significantly higher surface area than Cu/Nb<sub>2</sub>O<sub>5</sub>/Al<sub>2</sub>O<sub>3</sub>, which is expected to result in a superior catalytic performance of the former compared to the latter. This advantageous characteristic of Cu/NaY has been attributed to the three-dimensional pore structure of zeolite NaY [55].



**Figure 4.** N<sub>2</sub> adsorption/desorption isotherms of the catalysts (a) Cu/NaY and (b) Cu/Nb<sub>2</sub>O<sub>5</sub>/Al<sub>2</sub>O<sub>3</sub>.**Table 2.** Textural parameters of the catalysts and precursors.

Sample	Surface area (m <sup>2</sup> g <sup>-1</sup> )	Pore volume (cm <sup>3</sup> g <sup>-1</sup> )	Micropore volume (cm <sup>3</sup> g <sup>-1</sup> )	Pore diameter (nm)
Nb <sub>2</sub> O <sub>5</sub>	71.73	0.37	0.32	8.24
NaY	588.49	0.1479	0.0281	1.74
Al <sub>2</sub> O <sub>3</sub>	99.26	0.1799	0,0389	7.24
Cu/NaY	210.4	0.118	0.1114	2.24
Cu/Nb <sub>2</sub> O <sub>5</sub> /Al <sub>2</sub> O <sub>3</sub>	26	0.0617	0.0106	9.56

The FTIR spectra of the synthesized catalysts and both Nb<sub>2</sub>O<sub>5</sub> and NaY supports are shown in Figure 5a,b, respectively. The band at approximately 3500 cm<sup>-1</sup>, observed in all spectra, reveals the presence of surface hydroxyl groups in these materials [26,56]. The main NaY vibration modes were identified as the strong band located at 1029 cm<sup>-1</sup> and the lower intensity band at 469 cm<sup>-1</sup>, which correspond to the internal vibrations of the tetrahedral units of the zeolite, while the bands identified at 1150, 794, and 570 cm<sup>-1</sup> were attributed to the external linkages between the (Si/Al)O<sub>4</sub> tetrahedra [57]. Sensitive bands did not show significant changes in the Cu/NaY spectrum compared to those of NaY. On the other hand, the band at 570 cm<sup>-1</sup>, attributed to the polyhedral ring in the zeolite structure, showed a slight alteration that may be associated with the binding of copper. According to previous studies, copper oxide (CuO) bands are present between the wavenumbers of 610 and 500 cm<sup>-1</sup> [57,58].

**Figure 5.** Infrared spectra of the catalysts (a) Cu/NaY and Cu/Nb<sub>2</sub>O<sub>5</sub>/Al<sub>2</sub>O<sub>3</sub> and of the precursors (b) NaY and Nb<sub>2</sub>O<sub>5</sub>.

The FTIR spectrum of Nb<sub>2</sub>O<sub>5</sub> (Figure 5b) shows strong and broad bands in the region between 500 and 900 cm<sup>-1</sup>. The band centered at 896 cm<sup>-1</sup> is attributed to the Nb-O stretching vibration and the band at 760 cm<sup>-1</sup> to the Nb-O-Nb vibration [59]. The narrower band at 1622 cm<sup>-1</sup> is attributed to water molecules adsorbed on the Nb<sub>2</sub>O<sub>5</sub> surface [60]. The presence of niobium pentoxide was confirmed by

the presence of its main vibration modes in the FTIR spectrum of the Cu/Nb<sub>2</sub>O<sub>5</sub>/Al<sub>2</sub>O<sub>3</sub> catalyst (Figure 5a). Alterations were also noted in the intensity of the two bands between 500 and 900 cm<sup>-1</sup>, and in the resolution between them, when compared to the Nb<sub>2</sub>O<sub>5</sub> spectrum. These changes are associated to the binding with copper, as we are once again referring to the region of copper oxide bands.

### 3.1.4. Temperature-Programmed Desorption (TPD)

Analyses of both catalysts by TPD-NH<sub>3</sub> are shown in Figure 6. The NH<sub>3</sub> desorption profiles for Cu/NaY and Cu/Nb<sub>2</sub>O<sub>5</sub>/Al<sub>2</sub>O<sub>3</sub> were confined to the 140°C to 460°C and 150°C to 620°C temperatures ranges, respectively, showing that the support type influenced the acidity of the catalyst. The peak location and wide temperature range for Cu/NaY suggest the presence of sites of weak and intermediate acid strength. By contrast, the higher temperature range for Cu/Nb<sub>2</sub>O<sub>5</sub>/Al<sub>2</sub>O<sub>3</sub> is attributable to the presence of intermediate to strong acid sites. Also, Cu/NaY had a higher concentration of acid sites compared to Cu/Nb<sub>2</sub>O<sub>5</sub>/Al<sub>2</sub>O<sub>3</sub> (Table 3). In general, the higher acidity of Cu/NaY may be justified by its higher surface area.

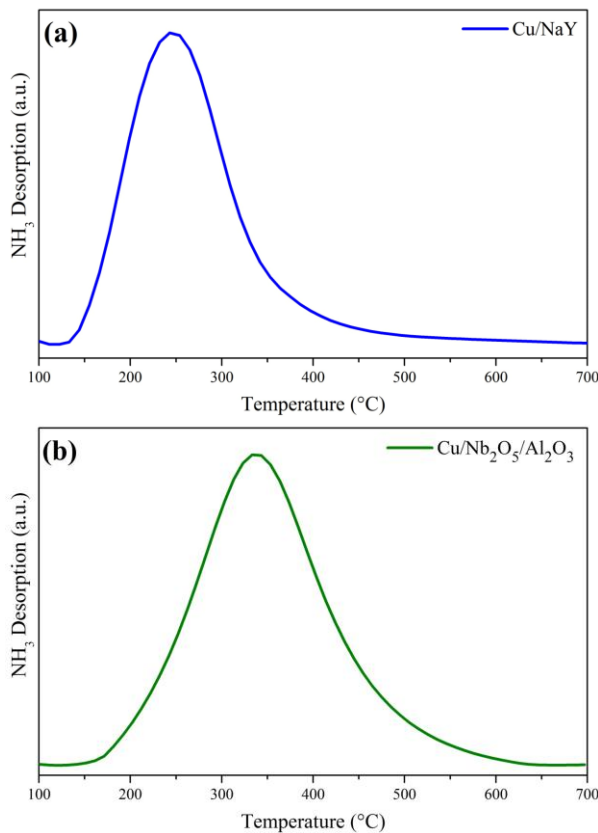


**Figure 6.** NH<sub>3</sub> desorption curves of the catalysts (a) Cu/NaY and (b) Cu/Nb<sub>2</sub>O<sub>5</sub>/Al<sub>2</sub>O<sub>3</sub>.

**Table 3.** Acidity of the synthesized catalysts by TPD-NH<sub>3</sub>.

Sample	Chemisorbed NH <sub>3</sub> (mmol/g)	Temperature (°C)
Cu/NaY	1.598	247
Cu/Nb <sub>2</sub> O <sub>5</sub> /Al <sub>2</sub> O <sub>3</sub>	0.059	336

The maximum NH<sub>3</sub> desorption temperature for the Cu/NaY catalyst was slightly higher than that for NaY alone, which typically ranges between 150°C and 250°C [61–63]. This is an indication that the incorporation of Cu into the zeolite structure increased the strength of its acid sites. On the other hand, the impregnation of Cu onto Nb<sub>2</sub>O<sub>5</sub>/Al<sub>2</sub>O<sub>3</sub> did not have a significant influence on the desorption temperature range.

### 3.1.5. Temperature-Programmed Reduction (TPR)

Both catalysts displayed a wide reduction range in their TPR profiles (Figure 7). However, the position of the maximum reduction temperature of CuO for Cu/Nb<sub>2</sub>O<sub>5</sub>/Al<sub>2</sub>O<sub>3</sub> was shifted to higher values compared to Cu/NaY, which may indicate a greater interaction of Cu with Nb<sub>2</sub>O<sub>5</sub>/Al<sub>2</sub>O<sub>3</sub> compared to NaY. Reduction at temperatures below 300°C indicated that CuO was dispersed on the catalyst surface with little interaction with the support. Above this temperature, total copper reduction was prevented in both catalytic systems by the interaction between CuO and the support surface [17,64]. Additionally, Cu/Nb<sub>2</sub>O<sub>5</sub>/Al<sub>2</sub>O<sub>3</sub> showed a reduction peak with a maximum around 928°C, which was attributed to the partial reduction of Nb<sub>2</sub>O<sub>5</sub> to NbO<sub>2</sub> [43,65]. The hydrogen consumption of the Cu/NaY catalyst was 6.16 mmol/g<sub>cat</sub>, while that of Cu/Nb<sub>2</sub>O<sub>5</sub>/Al<sub>2</sub>O<sub>3</sub> was 6.38 mmol/g<sub>cat</sub>, a slightly higher value due to the partial reduction of Nb<sub>2</sub>O<sub>5</sub>.

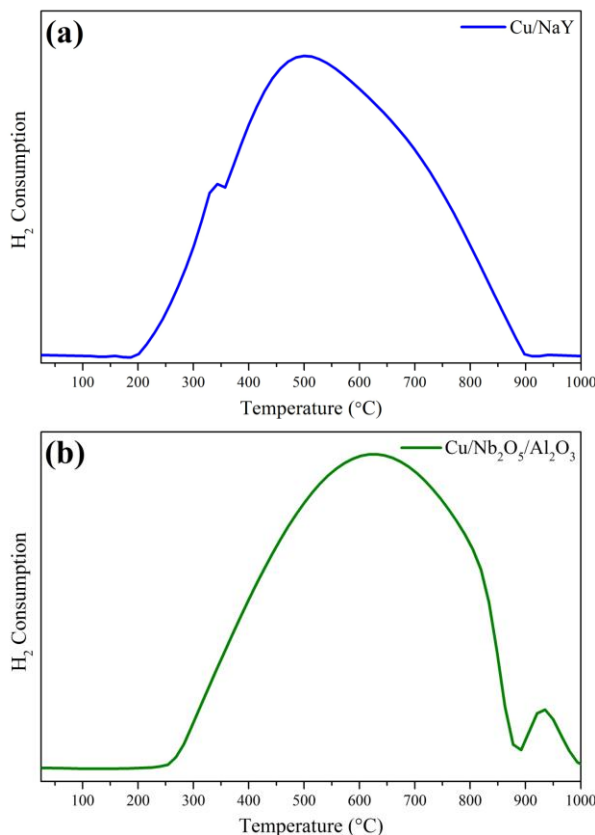


**Figure 7.** TPR profiles of (a) Cu/NaY and (b) Cu/Nb<sub>2</sub>O<sub>5</sub>/Al<sub>2</sub>O<sub>3</sub> catalysts.

### 3.2. Catalytic Performance Evaluation

Figure 8 shows the selectivity data for both Cu/Nb<sub>2</sub>O<sub>5</sub>/Al<sub>2</sub>O<sub>3</sub> and Cu/NaY at 300°C and 450°C. The differences between catalytic performances show that both support and temperature influenced the reaction efficiency. Conversion increased with increasing temperature for both catalysts, but the effect was more pronounced for the Cu/Nb<sub>2</sub>O<sub>5</sub>/Al<sub>2</sub>O<sub>3</sub> catalyst. On the other hand, the selectivity for H<sub>2</sub> and acetaldehyde decreased with increasing temperature, and the quantity of by-products (especially ethylene) increased, with this effect being greater for the Cu/Nb<sub>2</sub>O<sub>5</sub>/Al<sub>2</sub>O<sub>3</sub> catalyst.

For both catalysts at 300°C, the main reaction was ethanol dehydrogenation (Eq. 4) forming acetaldehyde and H<sub>2</sub>, while higher temperatures favored dehydration forming ethylene (Eq. 5). Also, the use of NaY at 450°C favored parallel reactions forming CO and CH<sub>4</sub> [30]. This is probably due to the presence of more pronounced acid sites in the zeolyte at lower temperatures, as observed by TPD-NH<sub>3</sub> analysis of the Cu/NaY catalyst, where acid sites are found between 100 and 450°C (Figure 6). Also, the high surface area of this catalyst contributed to the greater exposure of acid sites, as well as the catalytically active copper sites on the catalyst surface, promoting parallel reactions that are part

of the ethanol reforming reaction pathway. This explains the detection of reaction intermediates such as acetaldehyde.

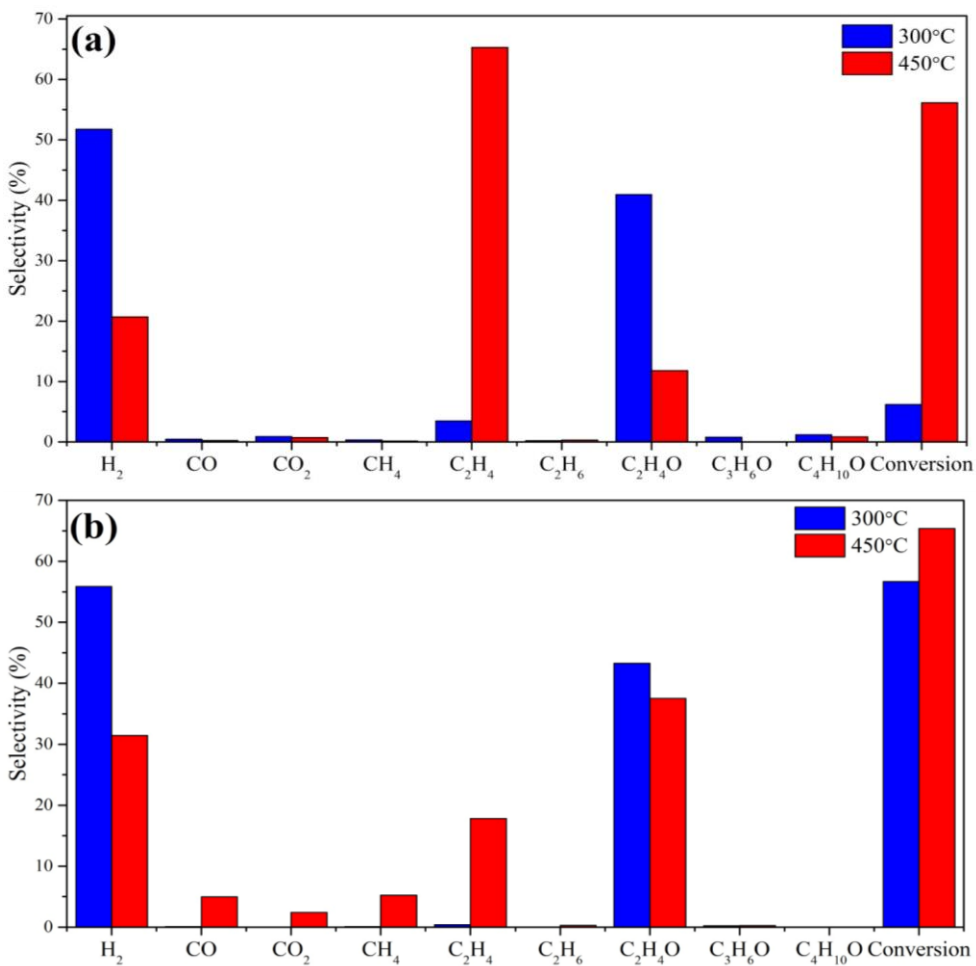


**Figure 8.** Average selectivity of (a) Cu/Nb<sub>2</sub>O<sub>5</sub>/Al<sub>2</sub>O<sub>3</sub> and (b) Cu/NaY at 300°C and 450°C.

The selectivity of Cu/Nb<sub>2</sub>O<sub>5</sub>/Al<sub>2</sub>O<sub>3</sub> to C<sub>2</sub>H<sub>4</sub> was higher than that of Cu/NaY. The TPD-NH<sub>3</sub> of this catalyst showed acid sites of greater strength due to the desorption of NH<sub>3</sub> at higher temperatures, which may be connected to the higher formation of C<sub>2</sub>H<sub>4</sub> [65]. Lorenzut et al. [66] observed the same low selectivity behavior for Cu catalysts supported on ZnO/Al<sub>2</sub>O<sub>3</sub>. Also, the support seemed to have influenced the reaction pathway, since Nb<sub>2</sub>O<sub>5</sub> is an n-type semiconductor that may have driven the selectivity toward ethanol and water. For the Cu/Nb<sub>2</sub>O<sub>5</sub>/Al<sub>2</sub>O<sub>3</sub> catalyst, the formation of CO<sub>2</sub> was limited at both temperatures, while for Cu/NaY, CO<sub>2</sub> formation was more pronounced at 450°C, indicating the occurrence of ethanol reforming.

Both catalysts exhibited more stability at 300°C (Figure 9) because, at 450°C, C<sub>2</sub>H<sub>4</sub> formation accelerated deactivation by coke deposition [67]. Overall, the results highlight the strong influence of the catalytic support on the steam reforming of ethanol for H<sub>2</sub> production. The Cu/NaY catalyst showed higher ethanol conversion compared to Cu/Nb<sub>2</sub>O<sub>5</sub>/Al<sub>2</sub>O<sub>3</sub>, suggesting that support properties such as surface area, pore volume, and pore size significantly influenced the catalytic performance. The porous structure and higher surface area of NaY may have facilitated copper dispersion and interaction with the reactants, enhancing the catalytic activity. Additionally, zeolites have a structure with a regular arrangement of uniform micropores that promote greater selectivity for H<sub>2</sub> formation.

Furthermore, the acidity measurements revealed that the incorporation of copper into NaY increases the strength of the acid sites, as indicated by the higher desorption temperature found for Cu/NaY compared to pure NaY in other studies [68–70]. This increased acidity may have contributed to the improvement of the catalytic activity by influencing the adsorption and breakdown of ethanol molecules. Therefore, a careful selection of the support is crucial for optimizing the performance of copper catalysts in H<sub>2</sub> production by SRE.

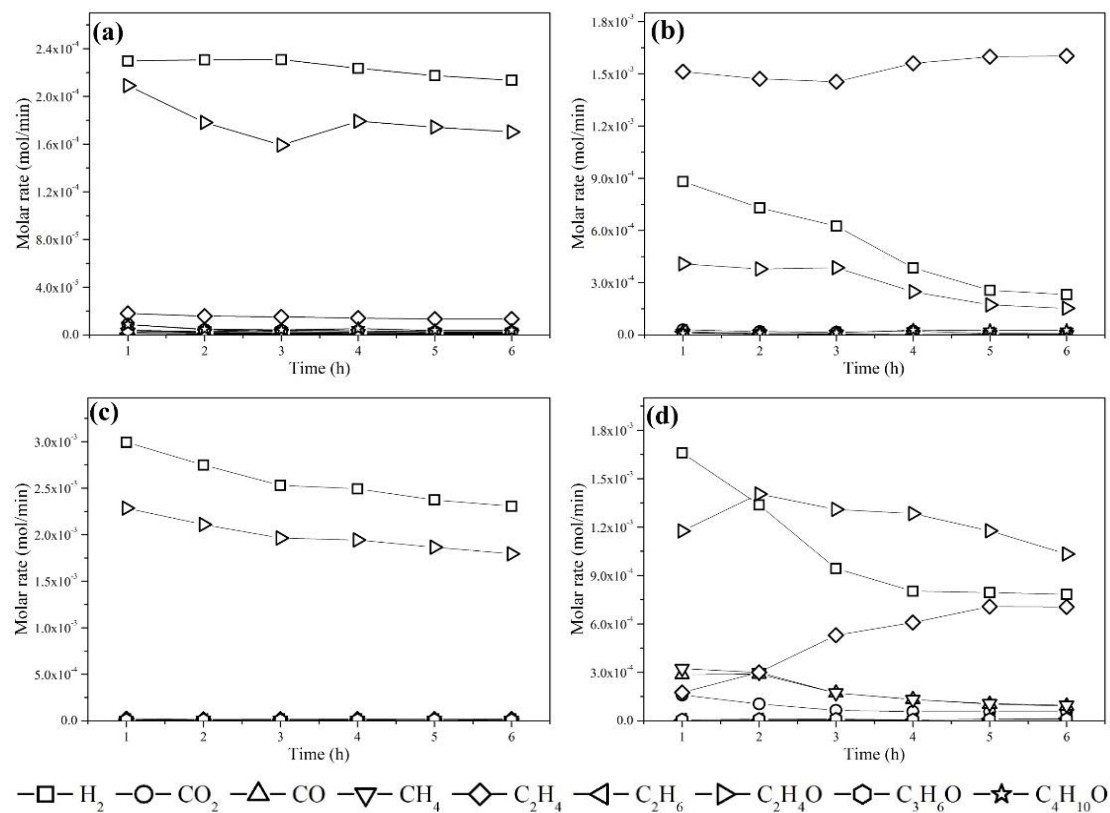


**Figure 9.** Molar rate as a function of time for Cu/Nb<sub>2</sub>O<sub>5</sub>/Al<sub>2</sub>O<sub>3</sub> at (a) 300°C and (b) 450°C and Cu/NaY at (c) 300°C and (d) 450°C.

The maximum H<sub>2</sub> production with the Cu/NaY catalyst, considering the average H<sub>2</sub> production rate of 0.57 mL/s at 450°C, was  $4.7 \times 10^{-5}$  g/s, regardless of the reaction pathway whereby H<sub>2</sub> was formed. Since the calorific value of H<sub>2</sub> is 142 kJ/g, this H<sub>2</sub> production represents 6.6 W for a catalyst mass of 5 g, or 1.33 W/g<sub>cat</sub>. Hence, 1.5 kg Cu/NaY would be required to power a 1 kW cell with an efficiency of 50%.

#### 4. Conclusions

The steam reforming of ethanol was viable using copper-based catalysts supported on NaY zeolite (Cu/NaY) and niobium-aluminum oxides (Cu/Nb<sub>2</sub>O<sub>5</sub>/Al<sub>2</sub>O<sub>3</sub>). The physicochemical properties of the two catalysts were different due to differences in the support properties. Nevertheless, copper particles were well dispersed in both catalysts, contributing to achieving better catalytic performances. Both catalysts were active in the steam reforming of ethanol, but Cu/NaY was best for H<sub>2</sub> production at 450°C, with CO<sub>2</sub> formation remaining constant throughout the reaction course. Therefore, this catalyst has potential for large-scale operations and, with the addition of a small amount of acidity dopants, it may become even more selective for H<sub>2</sub> production by ethanol reforming. Finally, the support effect was demonstrated as a relevant parameter for optimal SRE catalytic performance.

**Author Contributions:** Conceptualization, R.D., L.P.R. and M.S.; methodology, R.D., A.D.G. and B.R.F.; investigation, A.D.G. and B.R.F.; resources, L.P.R., M.S. and R.D.; data curation, R.P.N., P.D.M., A.D.G. and B.R.F.; writing—original draft preparation, P.D.M., R.P.N., R.D. and A.D.G.; writing—review and editing, P.D.M., R.P.N., A.D.G., L.P.R. and R.D.; supervision, R.D and L.P.R.; funding acquisition, L.P.R. All authors have read and agreed to the published version of the manuscript.

**Acknowledgments:** The authors would like to thank the support of the Multi-User Materials Characterization Center (CMCM) at the Federal Technological University of Paraná (UTFPR), the Department of Soils at the Agrarian Sciences Campus of the Federal University of Paraná (UFPR), the Companhia Brasileira de Metalurgia e Mineração (CBMM, Minas Gerais, Brazil); the Multi-User Laboratory of Chemical Analysis (LAMAQ) at the Federal Technological University of Paraná (UTFPR) for spectroscopy facilities; and the Catalysis Laboratory (LabCat) at the State University of Maringá (UEM). Also, the authors are grateful to the financial support of Conselho Nacional de Desenvolvimento Científico e Tecnológico (CNPq, Brazil - grant number 315930/2021-7), Fundação Araucária (grant agreement 002/2021, process #17.521.887-4 – NAPI-HCR project) and Coordenação de Aperfeiçoamento de Pessoal de Nível Superior (CAPES, Brazil - Finance Code 001).

**Conflicts of Interest:** The authors declare no conflicts of interest.

## References

1. Luo, M.; Li, S.; Di, Z.; Yang, Z.; Chou, W.; Shi, B. Fischer-Tropsch Synthesis: Effect of Nitric Acid Pretreatment on Graphene-Supported Cobalt Catalyst. *Appl Catal A Gen* **2020**, *599*, 117608, doi:10.1016/j.apcata.2020.117608.
2. Yousefian, F.; Babatabar, M.A.; Eshaghi, M.; Poor, S.M.; Tavasoli, A. Pyrolysis of Rice Husk, Coconut Shell, and Cladophora Glomerata Algae and Application of the Produced Biochars as Support for Cobalt Catalyst in Fischer-Tropsch Synthesis. *Fuel Processing Technology* **2023**, *247*, 107818, doi:10.1016/j.fuproc.2023.107818.
3. Liu, Y.; Zou, R.; Qin, B.; Gan, J.; Peng, X. Energy-Efficient Monosaccharides Electrooxidation Coupled with Green Hydrogen Production by Bifunctional Co9S8/Ni3S2 Electrode. *Chemical Engineering Journal* **2022**, *446*, 136950, doi:10.1016/j.cej.2022.136950.
4. Mert, M.E.; Edis, C.; Akyıldız, Ş.; Demir, B.N.; Nazligul, H.; Gurdal, Y.; Doğru Mert, B. Design and Performance Analysis of a PV-Assisted Alkaline Electrolysis for Hydrogen Production: An Experimental and Theoretical Study. *Fuel* **2024**, *355*, 129497, doi:10.1016/j.fuel.2023.129497.
5. Vadalà, M.; Kröll, E.; Küppers, M.; Lupascu, D.C.; Brunstermann, R. Hydrogen Production via Dark Fermentation by Bacteria Colonies on Porous PDMS-Scaffolds. *Int J Hydrogen Energy* **2023**, *48*, 25274–25284, doi:10.1016/j.ijhydene.2023.03.285.
6. Öztan, H.; Çapoğlu, İ.K.; Uysal, D.; Doğan, Ö.M. A Parametric Study to Optimize the Temperature of Hazelnut and Walnut Shell Gasification for Hydrogen and Methane Production. *Bioresour Technol Rep* **2023**, *23*, 101581, doi:10.1016/j.biteb.2023.101581.
7. Guan, D.; Wang, F.; Zhang, X.; Dou, W.; Sun, Y. Comprehensive Study on Catalytic Coating Tubular Reactor with Electromagnetic Induction Heating for Hydrogen Production through Methanol Steam Reforming. *Int J Hydrogen Energy* **2024**, *50*, 1–17, doi:10.1016/j.ijhydene.2023.07.316.
8. Hu, Y.; He, W.; Shen, Y. Recyclable NiMnO<sub>x</sub>/NaF Catalysts: Hydrogen Generation via Steam Reforming of Formaldehyde. *Fuel* **2023**, *354*, 129311, doi:10.1016/j.fuel.2023.129311.
9. Levikhin, A.A.; Boryaev, A.A. High-Temperature Reactor for Hydrogen Production by Partial Oxidation of Hydrocarbons. *Int J Hydrogen Energy* **2023**, *48*, 28187–28204, doi:10.1016/j.ijhydene.2023.03.459.
10. da Silva, F.A.; Dancini-Pontes, I.; DeSouza, M.; Fernandes, N.R.C. Kinetics of Ethanol Steam Reforming over Cu–Ni/Nb<sub>x</sub>O<sub>y</sub> Catalyst. *Reaction Kinetics, Mechanisms and Catalysis* **2017**, *122*, 557–574, doi:10.1007/s11144-017-1210-2.
11. Shtyka, O.; Dimitrova, Z.; Ciesielski, R.; Kedziora, A.; Mitukiewicz, G.; Leyko, J.; Maniukiewicz, W.; Czylkowska, A.; Maniecki, T. Steam Reforming of Ethanol for Hydrogen Production: Influence of Catalyst Composition (Ni/Al<sub>2</sub>O<sub>3</sub>, Ni/Al<sub>2</sub>O<sub>3</sub>–CeO<sub>2</sub>, Ni/Al<sub>2</sub>O<sub>3</sub>–ZnO) and Process Conditions. *Reaction Kinetics, Mechanisms and Catalysis* **2021**, *132*, 907–919, doi:10.1007/s11144-021-01945-6.
12. Haryanto, A.; Fernando, S.; Murali, N.; Adhikari, S. Current Status of Hydrogen Production Techniques by Steam Reforming of Ethanol: A Review. *Energy & Fuels* **2005**, *19*, 2098–2106, doi:10.1021/ef0500538.
13. Zanchet, D.; Santos, J.B.O.; Damyanova, S.; Gallo, J.M.R.; Bueno, J.M.C. Toward Understanding Metal-Catalyzed Ethanol Reforming. *ACS Catal* **2015**, *5*, 3841–3863, doi:10.1021/cs5020755.
14. Trane-Restrup, R.; Dahl, S.; Jensen, A.D. Steam Reforming of Ethanol: Effects of Support and Additives on Ni-Based Catalysts. *Int J Hydrogen Energy* **2013**, *38*, 15105–15118, doi:10.1016/j.ijhydene.2013.09.027.
15. Wurzler, G.T.; Rabelo-Neto, R.C.; Mattos, L. V.; Fraga, M.A.; Noronha, F.B. Steam Reforming of Ethanol for Hydrogen Production over MgO–Supported Ni-Based Catalysts. *Appl Catal A Gen* **2016**, *518*, 115–128, doi:10.1016/j.apcata.2015.11.020.

16. Palma, V.; Ruocco, C.; Castaldo, F.; Ricca, A.; Boettge, D. Ethanol Steam Reforming over Bimetallic Coated Ceramic Foams: Effect of Reactor Configuration and Catalytic Support. *Int J Hydrogen Energy* **2015**, *40*, 12650–12662, doi:10.1016/j.ijhydene.2015.07.138.
17. Alonso, C.G.; Furtado, A.C.; Cantão, M.P.; Andreo dos Santos, O.A.; Camargo Fernandes-Machado, N.R. Reactions over Cu/Nb<sub>2</sub>O<sub>5</sub> Catalysts Promoted with Pd and Ru during Hydrogen Production from Ethanol. *Int J Hydrogen Energy* **2009**, *34*, 3333–3341, doi:10.1016/j.ijhydene.2009.02.021.
18. Chen, F.; Tao, Y.; Ling, H.; Zhou, C.; Liu, Z.; Huang, J.; Yu, A. Ni-Cu Bimetallic Catalysts on Yttria-Stabilized Zirconia for Hydrogen Production from Ethanol Steam Reforming. *Fuel* **2020**, *280*, 118612, doi:10.1016/j.fuel.2020.118612.
19. Ranjekar, A.M.; Yadav, G.D. Steam Reforming of Ethanol for Hydrogen Production: Efficacy of Ceria Promoted Cu-Co on Mesoporous Cellular Foam Silica. *Int J Hydrogen Energy* **2023**, *48*, 31550–31570, doi:10.1016/j.ijhydene.2023.04.276.
20. Guarido, C.E.M.; Cesar, D. V.; Souza, M.M.V.M.; Schmal, M. Ethanol Reforming and Partial Oxidation with Cu/Nb<sub>2</sub>O<sub>5</sub> Catalyst. *Catal Today* **2009**, *142*, 252–257, doi:10.1016/j.cattod.2008.08.030.
21. Hou, T.; Zhang, S.; Chen, Y.; Wang, D.; Cai, W. Hydrogen Production from Ethanol Reforming: Catalysts and Reaction Mechanism. *Renewable and Sustainable Energy Reviews* **2015**, *44*, 132–148, doi:10.1016/j.rser.2014.12.023.
22. Mariño, F.J.; Cerrella, E.G.; Duhalde, S.; Jobbagy, M.; Laborde, M.A. Hydrogen from Steam Reforming of Ethanol. Characterization and Performance of Copper-Nickel Supported Catalysts. *Int J Hydrogen Energy* **1998**, *23*, 1095–1101, doi:10.1016/S0360-3199(97)00173-0.
23. Ni, M.; Leung, D.Y.C.; Leung, M.K.H. A Review on Reforming Bio-Ethanol for Hydrogen Production. *Int J Hydrogen Energy* **2007**, *32*, 3238–3247, doi:10.1016/j.ijhydene.2007.04.038.
24. Snytnikov, P.V.; Badmaev, S.D.; Volkova, G.G.; Potemkin, D.I.; Zyryanova, M.M.; Belyaev, V.D.; Sobyanin, V.A. Catalysts for Hydrogen Production in a Multifuel Processor by Methanol, Dimethyl Ether and Bioethanol Steam Reforming for Fuel Cell Applications. *Int J Hydrogen Energy* **2012**, *37*, 16388–16396, doi:10.1016/j.ijhydene.2012.02.116.
25. Inokawa, H.; Nishimoto, S.; Kameshima, Y.; Miyake, M. Difference in the Catalytic Activity of Transition Metals and Their Cations Loaded in Zeolite Y for Ethanol Steam Reforming. *Int J Hydrogen Energy* **2010**, *35*, 11719–11724, doi:10.1016/j.ijhydene.2010.08.092.
26. Nippes, R.P.; Frederichi, D.; Olsen Scaliante, e M.H.N. Enhanced Photocatalytic Performance under Solar Radiation of ZnO through Hetero-Junction with Iron Functionalized Zeolite. *J Photochem Photobiol A Chem* **2021**, *418*, 113373, doi:10.1016/j.jphotochem.2021.113373.
27. Mohamed, R.M.; Mkhaldid, I.A.; Barakat, M.A. Rice Husk Ash as a Renewable Source for the Production of Zeolite NaY and Its Characterization. *Arabian Journal of Chemistry* **2015**, *8*, 48–53, doi:10.1016/j.arabjc.2012.12.013.
28. Tolentino, C.M.C.; de Luna, M.D.G.; Futalan, C.M.; Choi, A.E.S.; Manegdeg, F.G.; Grisdanurak, N. Influence of Hydrocarbons on Hydrogen Chloride Removal from Refinery Off-Gas by Zeolite NaY Derived from Rice Husks. *Science of The Total Environment* **2020**, *728*, 138782, doi:10.1016/j.scitotenv.2020.138782.
29. Ali, M.M.M.; Ahmed, M.J.; Hameed, B.H. NaY Zeolite from Wheat (*Triticum Aestivum L.*) Straw Ash Used for the Adsorption of Tetracycline. *J Clean Prod* **2018**, *172*, 602–608, doi:10.1016/j.jclepro.2017.10.180.
30. Campos-Skrobot, F.C.; Rizzo-Domingues, R.C.P.; Fernandes-Machado, N.R.C.; Cantão, M.P. Novel Zeolite-Supported Rhodium Catalysts for Ethanol Steam Reforming. *J Power Sources* **2008**, *183*, 713–716, doi:10.1016/j.jpowsour.2008.05.066.
31. Kwak, B.S.; Lee, J.S.; Lee, J.S.; Choi, B.-H.; Ji, M.J.; Kang, M. Hydrogen-Rich Gas Production from Ethanol Steam Reforming over Ni/Ga/Mg/Zeolite Y Catalysts at Mild Temperature. *Appl Energy* **2011**, *88*, 4366–4375, doi:10.1016/j.apenergy.2011.05.017.
32. Lee, J.-S.; Kim, J.-E.; Kang, M.-S. Hydrogen Production from Ethanol Steam Reforming over SnO<sub>2</sub> - K<sub>2</sub>O/Zeolite Y Catalyst. *Bull Korean Chem Soc* **2011**, *32*, 1912–1920, doi:10.5012/bkcs.2011.32.6.1912.
33. Androulakis, A.; Yentekakis, I.V.; Panagiotopoulou, P. Dry Reforming of Methane over Supported Rh and Ru Catalysts: Effect of the Support (Al<sub>2</sub>O<sub>3</sub>, TiO<sub>2</sub>, ZrO<sub>2</sub>, YSZ) on the Activity and Reaction Pathway. *Int J Hydrogen Energy* **2023**, *48*, 33886–33902, doi:10.1016/j.ijhydene.2023.03.114.
34. Kharaji, A.G.; Shariati, A.; Takassi, M.A. A Novel  $\gamma$ -Alumina Supported Fe-Mo Bimetallic Catalyst for Reverse Water Gas Shift Reaction. *Chin J Chem Eng* **2013**, *21*, 1007–1014, doi:10.1016/S1004-9541(13)60573-X.
35. Pastor-Pérez, L.; Shah, M.; le Saché, E.; Ramirez Reina, T. Improving Fe/Al<sub>2</sub>O<sub>3</sub> Catalysts for the Reverse Water-Gas Shift Reaction: On the Effect of Cs as Activity/Selectivity Promoter. *Catalysts* **2018**, *8*, 608, doi:10.3390/catal8120608.
36. Ranjbar, A.; Aghamiri, S.F.; Irankhah, A. Effect of MgO/Al<sub>2</sub>O<sub>3</sub> Ratio in the Support of Mesoporous Ni/MgO-Al<sub>2</sub>O<sub>3</sub> Catalysts for CO<sub>2</sub> Utilization via Reverse Water Gas Shift Reaction. *Int J Hydrogen Energy* **2023**, *48*, 19115–19125, doi:10.1016/j.ijhydene.2023.01.102.

37. Xiao, T.; Xie, J.; Cheng, J.; Dai, X.; Lu, S.; Zuo, R.; Li, Z.; Yang, Z.  $\text{Al}_2\text{O}_3$  Supported NiCu Alloy as a Stable Catalyst for Selective Hydrogenation of Phthalic Anhydride to Phthalide. *Appl Catal A Gen* **2023**, *660*, 119189, doi:10.1016/j.apcata.2023.119189.

38. Yao, X.; Gao, F.; Dong, L. The Application of Incorporation Model in  $\gamma\text{-Al}_2\text{O}_3$  Supported Single and Dual Metal Oxide Catalysts: A Review. *Chinese Journal of Catalysis* **2013**, *34*, 1975–1985, doi:10.1016/S1872-2067(12)60708-6.

39. Ji, N.; Yin, J.; Rong, Y.; Li, H.; Yu, Z.; Lei, Y.; Wang, S.; Diao, X. More than a Support: The Unique Role of  $\text{Nb}_2\text{O}_5$  in Supported Metal Catalysts for Lignin Hydrodeoxygenation. *Catal Sci Technol* **2022**, *12*, 3751–3766, doi:10.1039/D2CY00245K.

40. Zhang, C.; Wu, J.; Hua, C.; Zhu, L.; Qiu, K.; Wang, S. Hydrodeoxygenation Performance of Lignin-Derived Phenolics to Cycloalkanes: Insights into the Crystal Structures of the  $\text{Nb}_2\text{O}_5$  Support. *Energy & Fuels* **2023**, *37*, 14006–14020, doi:10.1021/acs.energyfuels.3c02083.

41. Nippes, R.P.; Gomes, A.D.; Macruz, P.D.; de Souza, M. Photocatalytic Removal of  $17\beta$ -Estradiol from Water Using a Novel Bimetallic NiCu/ $\text{Nb}_2\text{O}_5$  Catalyst. *Environmental Science and Pollution Research* **2023**, *30*, 103731–103742, doi:10.1007/s11356-023-29727-8.

42. Nippes, R.P.; Macruz, P.D.; Gomes, A.D.; Girotto, C.P.; Scaliante, M.H.N.O.; de Souza, M. Removal of Reactive Blue 250 Dye from Aqueous Medium Using Cu/Fe Catalyst Supported on  $\text{Nb}_2\text{O}_5$  through Oxidation with  $\text{H}_2\text{O}_2$ . *Reaction Kinetics, Mechanisms and Catalysis* **2022**, *135*, 2697–2717, doi:10.1007/s11144-022-02279-7.

43. Dancini-Pontes, I.; DeSouza, M.; Silva, F.A.; Scaliante, M.H.N.O.; Alonso, C.G.; Bianchi, G.S.; Medina-Neto, A.; Pereira, G.M.; Fernandes-Machado, N.R.C. Influence of the  $\text{CeO}_2$  and  $\text{Nb}_2\text{O}_5$  Supports and the Inert Gas in Ethanol Steam Reforming for H<sub>2</sub> Production. *Chemical Engineering Journal* **2015**, *273*, 66–74, doi:10.1016/j.cej.2015.03.032.

44. Menezes, J.P. da S.Q.; Manfro, R.L.; Souza, M.M.V.M. Hydrogen Production from Glycerol Steam Reforming over Nickel Catalysts Supported on Alumina and Niobia: Deactivation Process, Effect of Reaction Conditions and Kinetic Modeling. *Int J Hydrogen Energy* **2018**, *43*, 15064–15082, doi:10.1016/j.ijhydene.2018.06.048.

45. Mortezaei, Z.; Zendehdel, M.; Bodaghifard, M.A. Cu Complex Grafted on the Porous Materials: Synthesis, Characterization and Comparison of Their Antibacterial Activity with Nano-Cu/NaY Zeolite. *Journal of the Iranian Chemical Society* **2020**, *17*, 283–295, doi:10.1007/s13738-019-01769-1.

46. Gonçalves, J.F.; Souza, M.M.V.M. Ni/X% $\text{Nb}_2\text{O}_5$ / $\text{Al}_2\text{O}_3$  Catalysts Prepared via Coprecipitation-Wet Impregnation Method for Methane Steam Reforming. *Current Catalysis* **2020**, *9*, 80–89, doi:10.2174/2211544708666190423130340.

47. Kugai, J.; Subramani, V.; Song, C.; Engelhard, M.; Chin, Y. Effects of Nanocrystalline  $\text{CeO}_2$  Supports on the Properties and Performance of Ni-Rh Bimetallic Catalyst for Oxidative Steam Reforming of Ethanol. *J Catal* **2006**, *238*, 430–440, doi:10.1016/j.jcat.2006.01.001.

48. Thommes, M.; Kaneko, K.; Neimark, A. V.; Olivier, J.P.; Rodriguez-Reinoso, F.; Rouquerol, J.; Sing, K.S.W. Physisorption of Gases, with Special Reference to the Evaluation of Surface Area and Pore Size Distribution (IUPAC Technical Report). *Pure and Applied Chemistry* **2015**, *87*, 1051–1069, doi:10.1515/PAC-2014-1117/MACHINEREADABLECITATION/RIS.

49. Beltrame, K.K.; Cazetta, A.L.; de Souza, P.S.C.; Spessato, L.; Silva, T.L.; Almeida, V.C. Adsorption of Caffeine on Mesoporous Activated Carbon Fibers Prepared from Pineapple Plant Leaves. *Ecotoxicol Environ Saf* **2018**, *147*, 64–71, doi:10.1016/j.ecotox.2017.08.034.

50. Zhang, H.; Liu, X.; He, G.; Zhang, X.; Bao, S.; Hu, W. Bioinspired Synthesis of Nitrogen/Sulfur Co-Doped Graphene as an Efficient Electrocatalyst for Oxygen Reduction Reaction. *J Power Sources* **2015**, *279*, 252–258, doi:10.1016/j.jpowsour.2015.01.016.

51. Patdhanagul, N.; Srithanratana, T.; Rangsriwatananon, K.; Hengrasmee, S. Ethylene Adsorption on Cationic Surfactant Modified Zeolite NaY. *Microporous and Mesoporous Materials* **2010**, *131*, 97–102, doi:10.1016/j.micromeso.2009.12.008.

52. Zeng, Y.; Walker, H.; Zhu, Q. Reduction of Nitrate by NaY Zeolite Supported Fe, Cu/Fe and Mn/Fe Nanoparticles. *J Hazard Mater* **2017**, *324*, 605–616, doi:10.1016/j.jhazmat.2016.11.032.

53. Chang, H.-Y.; Lai, G.-H.; Tsai, D.-H. Aerosol Route Synthesis of Ni- $\text{CeO}_2$ - $\text{Al}_2\text{O}_3$  Hybrid Nanoparticle Cluster for Catalysis of Reductive Amination of Polypropylene Glycol. *Advanced Powder Technology* **2019**, *30*, 2293–2298, doi:10.1016/j.apt.2019.07.009.

54. Fawaz, A.; Bizreh, Y.W.; Al-Hamoud, L. (NiO, Ag / $\text{Fe}_2\text{O}_3$ - $\text{Al}_2\text{O}_3$ -Bentonite) as Promising Catalyst for CO and HC Removal from Single-Cylinder Engine Exhaust Emissions. *Catal Commun* **2022**, *171*, 106521, doi:10.1016/j.catcom.2022.106521.

55. Morales-Pacheco, P.; Alvarez, F.; Bucio, L.; Domínguez, J.M. Synthesis and Structural Properties of Zeolitic Nanocrystals II: FAU-Type Zeolites. *The Journal of Physical Chemistry C* **2009**, *113*, 2247–2255, doi:10.1021/jp8070713.

56. Ameri, A.; Faramarzi, M.A.; Tarighi, S.; Shakibaie, M.; Ameri, A.; Ramezani-Sarbandi, A.; Forootanfar, H. Removal of Dyes by *Trametes Versicolor* Laccase Immobilized on NaY-Zeolite. *Chemical Engineering Research and Design* **2023**, *197*, 240–253, doi:10.1016/j.cherd.2023.07.014.

57. El-Bahy, Z.M. Oxidation of Carbon Monoxide over Cu- and Ag-NaY Catalysts with Aqueous Hydrogen Peroxide. *Mater Res Bull* **2007**, *42*, 2170–2183, doi:10.1016/j.materresbull.2007.01.004.

58. Xu, Y.; Chen, D.; Jiao, X. Fabrication of CuO Pricky Microspheres with Tunable Size by a Simple Solution Route. *J Phys Chem B* **2005**, *109*, 13561–13566, doi:10.1021/jp051577b.

59. Khan, I.; Baig, N.; Qurashi, A. Graphitic Carbon Nitride Impregnated Niobium Oxide (g-C<sub>3</sub>N<sub>4</sub>/Nb<sub>2</sub>O<sub>5</sub>) Type (II) Heterojunctions and Its Synergetic Solar-Driven Hydrogen Generation. *ACS Appl Energy Mater* **2019**, *2*, 607–615, doi:10.1021/acsaem.8b01633.

60. da Conceição, L.R. V.; Carneiro, L.M.; Rivaldi, J.D.; de Castro, H.F. Solid Acid as Catalyst for Biodiesel Production via Simultaneous Esterification and Transesterification of Macaw Palm Oil. *Ind Crops Prod* **2016**, *89*, 416–424, doi:10.1016/j.indcrop.2016.05.044.

61. Fan, D.; Jiang, S.; Qiao, K.; Zhang, S.; Wang, H.; Bo, D.; Zhang, Y.; Yu, T.; Zhai, D.; Ren, G.; et al. Cuprous Species Distribution over CuCl/NaY Dependent on Acidity and Their CO Adsorption/Desorption Performance Study. *Chemical Engineering Journal* **2022**, *433*, 133763, doi:10.1016/j.cej.2021.133763.

62. Padró, C.L.; Rey, E.A.; González Peña, L.F.; Apesteguía, C.R. Activity, Selectivity and Stability of Zn-Exchanged NaY and ZSM5 Zeolites for the Synthesis of o-Hydroxyacetophenone by Phenol Acylation. *Microporous and Mesoporous Materials* **2011**, *143*, 236–242, doi:10.1016/j.micromeso.2011.03.005.

63. Wang, Z.; Ma, R.; Song, W. Influence of HSAPO-34, HZSM-5, and NaY on Pyrolysis of Corn Straw Fermentation Residue via Py-GC/MS. *J Anal Appl Pyrolysis* **2016**, *122*, 183–190, doi:10.1016/j.jaap.2016.09.025.

64. Ungureanu, A.; Dragoi, B.; Chiriac, A.; Ciotonea, C.; Royer, S.; Duprez, D.; Mamede, A.S.; Dumitriu, E. Composition-Dependent Morphostructural Properties of Ni–Cu Oxide Nanoparticles Confined within the Channels of Ordered Mesoporous SBA-15 Silica. *ACS Appl Mater Interfaces* **2013**, *5*, 3010–3025, doi:10.1021/am302733m.

65. da Silva, F.A.; Pontes, I.D.; Wurzler, G.T.; Alonso, C.G.; Medina-Neto, A.; Scaliante, M.H.N.O.; Desouza, M.; Fernandes-Machado, N.R.C. Production of Hydrogen from Bioethanol in Cu-Ni/NbxOy Catalysts Obtained by Different Preparation Methods. *Int J Hydrogen Energy* **2016**, *41*, 8111–8119, doi:10.1016/j.ijhydene.2015.12.215.

66. Lorenzut, B.; Montini, T.; De Rogatis, L.; Canton, P.; Benedetti, A.; Fornasiero, P. Hydrogen Production through Alcohol Steam Reforming on Cu/ZnO-Based Catalysts. *Appl Catal B* **2011**, *101*, 397–408, doi:10.1016/j.apcatb.2010.10.009.

67. Mattos, L. V.; Jacobs, G.; Davis, B.H.; Noronha, F.B. Production of Hydrogen from Ethanol: Review of Reaction Mechanism and Catalyst Deactivation. *Chem Rev* **2012**, *112*, 4094–4123, doi:10.1021/cr2000114.

68. Tang, S.; Li, F.; Liu, J.; Guo, B.; Tian, Z.; Lv, J. MgO/NaY as Modified Mesoporous Catalyst for Methanolysis of Polyethylene Terephthalate Wastes. *J Environ Chem Eng* **2022**, *10*, 107927, doi:10.1016/j.jece.2022.107927.

69. Boonyoung, P.; Thongratkaew, S.; Rungtaweevoranit, B.; Pengsawang, A.; Praserthdam, P.; Sanpitakseree, C.; Faungnawakij, K. Formic Acid as a Sacrificial Agent for Byproduct Suppression in Glucose Dehydration to 5-Hydroxymethylfurfural Using NaY Zeolite Catalyst. *Bioresour Technol* **2024**, *392*, 130010, doi:10.1016/j.biortech.2023.130010.

70. Nagpure, A.S.; Mohture, V.M.; Kayarkar, A. Green Synthesis of Highly Dispersed Cu Metal Nanoparticles Catalysts. *Inorg Chem Commun* **2022**, *146*, 110118, doi:10.1016/j.inoche.2022.110118.

**Disclaimer/Publisher's Note:** The statements, opinions and data contained in all publications are solely those of the individual author(s) and contributor(s) and not of MDPI and/or the editor(s). MDPI and/or the editor(s) disclaim responsibility for any injury to people or property resulting from any ideas, methods, instructions or products referred to in the content.